

# COMPLEXITY AT MESOSCALE

A. R. Bishop, K. Ø. Rasmussen, J. Röder, T. Lookman, and A. Saxena  
*Theoretical Division and Center for Nonlinear Studies, Los Alamos National Laboratory,  
Los Alamos, New Mexico 87545, USA*

Andrea Vanossi

*Dipartimento di Fisica, Università di Bologna, V.le Bertini Pichat 6/2, I-40127, Bologna,  
Italy, and INFN e Dipartimento di Fisica, Università di Modena, Via Campi 213/A,  
41100 Modena, Italy*

Panayotis Kevrekidis

*Program in Applied and Computational Mathematics, Princeton University, Fine Hall,  
Washington Road, Princeton, New Jersey, 08544-1000, USA*

**Keywords:** Pattern formation, multiscale phenomena, long-range effects.

**Abstract** Through three examples we illustrate some of the concepts and ingredients required for pattern formation at mesoscopic scales. Two examples build on microscopic models where mesoscopic patterns emerge from homogeneous ground states driven into instability by external forcing. In contrast, the third example builds on a mesoscopic phenomenological Ginzburg-Landau type model of solid-solid structural phase transitions. Here, mesoscopic textures emerge as a result of competing length scales arising from the constraints of elastic compatibility.

## 1. INTRODUCTION

Complex spatial patterns are typical observations in physical systems at mesoscales. Often such mesoscopic complex spatial patterns are observed in systems driven away from equilibrium or as results of phase transitions. By way of three examples, in the present paper we describe some of the ingredients that work together to create mesoscopic patterns. We will describe two quite different driven dynamical systems in which

the uniform ground state becomes unstable as the system is driven away from equilibrium. In both cases we illustrate how the instability through nonlinear, and long-range interactions gives rise to dynamically stable mesoscopic patterns consisting of locally coherent defect-like entities. To contrast these two examples we also discuss modeling of solid-solid structural phase transitions such as found in martensitic materials [1]. In the latter example our model builds on continuum elasticity in a phenomenological manner. In this case we will show how temperature (or pressure) driven structural phase transitions result in the emergence of mesoscopic textures in strain fields.

These three examples serve to illustrate several ingredients controlling mesoscopic patterns: driven versus undriven environments; the importance of discrete lattice scales; the competitions between (often anisotropic) short and long-range interactions; and the role of constraints as source of long-range interactions.

## 2. PATTERN FORMATION IN A DRIVEN NONLINEAR LATTICE

We will start with our simplest example [2], a driven damped Klein-Gordon lattice and consider it in some detail to introduce concepts. The explicit model is

$$\ddot{x}_n + \gamma \dot{x}_n + \omega_0^2 x_n = \Delta_n x_n + \lambda x_n^3 + \varepsilon \cos \omega t, \quad (1.1)$$

where  $\gamma$  is the damping parameter,  $\omega_0$  the natural frequency of the oscillators,  $\lambda = \pm 1$  the nonlinearity parameter, and, finally  $\varepsilon$  is the amplitude of the ac-drive at frequency  $\omega$ . In one spatial dimension the nearest neighbor coupling is  $\Delta_n x_n = x_{n+1} - 2x_n + x_{n-1}$  [3]. The amplitude  $A_0$  (and phase  $\delta_0$ ) of the spatially homogeneous solution  $x_n = y = A_0 \cos(\omega t + \delta_0)$  of Eq.(1.1) can, within the rotating wave approximation, be shown to satisfy

$$A_0^2 \left( \gamma^2 \omega^2 + (\omega^2 - \omega_0^2 + \frac{3}{4} \lambda A_0^2)^2 \right) = \varepsilon^2. \quad (1.2)$$

Analyzing the stability of the homogeneous solution with respect to spatial perturbations, we introduce  $x_n = y + z_n$  into Eq.(1.1). Assuming periodic boundary conditions, we may expand  $z_n$  in its Fourier components  $z_n = \sum_k \exp(ikn) \xi_k(t)$ , where the mode amplitude  $\xi_k(t)$  is then governed by

$$\ddot{\xi}_k + \gamma \dot{\xi}_k + \omega_k^2 \xi_k = \frac{3}{2} \lambda A_0^2 [1 + \cos(2\omega t + 2\delta_0)] \xi_k, \quad (1.3)$$

with  $\omega_k^2 = \omega_0^2 + 4 \sin^2(k/2)$  denoting the linear dispersion relation.

Finally, the transformation  $\xi_k(t) = \zeta_k(\omega t + \delta_0) \exp(-\frac{\gamma}{2}(\omega t + \delta)) \equiv \zeta_k(\tau) \exp(-\frac{\gamma}{2}\tau)$  reduces Eq.(1.3) to a standard Mathieu equation

$$\frac{d^2\zeta_k}{d\tau^2} + a\zeta_k - 2q \cos(2\tau)\zeta_k = 0, \quad (1.4)$$

where

$$a = \frac{1}{4\omega^2} (4\omega_k^2 - 6\lambda A_0^2 - \gamma^2), \quad q = \frac{3\lambda A_0^2}{4\omega^2}. \quad (1.5)$$

As is well-known [4], the Mathieu equation exhibits parametric resonances when  $\sqrt{a} \simeq i$ , where  $i = 1, 2, 3, \dots$ . The width of the resonance regions depends on the ratio  $q/a$  (see, e.g. Ref. [5]). In the framework of Eq.(1.4) the extent of the primary resonance  $a \simeq 1$  can easily be estimated [5] to be  $(a - 1)^2 < q^2$ . However, in the presence of the damping  $\gamma$  the resonance condition for Eq.(1.3) becomes

$$q^2 > \frac{\gamma^2}{\omega^2} + (a - 1)^2. \quad (1.6)$$

With  $a$  and  $q$  defined in Eqs. (1.5), given  $\lambda, \gamma, \omega, \omega_0$ , and  $\varepsilon$ , this translates into an instability band of certain wavenumbers  $k$ .

The above analysis is easily extended to the case of two spatial dimensions [3], the only required change being that the dispersion relation now is  $\omega_k^2 = \omega_0^2 + 4 \sin^2(k_x/2) + 4 \sin^2(k_y/2)$ , where the wavevector is  $\vec{k} = (k_x, k_y)$ . The instability in this case appears on an annulus in the wavevector plane, with a radius given by  $a = 1$  (see, Eq. (1.5)) and a width determined by Eq. (1.6)

Numerical simulations allow us to follow the full nonlinear development and saturation initiated by the linear instability itself. In particular, in regions of parameter space we obtain the spontaneous formation of patterns of distinct spatial geometry. Although we have studied this phenomenon in one as well as in two dimensions, in the present communication we focus on the two-dimensional system, where the pattern formation is particularly rich.

Although the dynamics show different features according to the specific region of parameter space, it is possible to trace a typical behavior as follows: Initializing the system in the spatially homogeneous state described above with a small amount of randomness added, the instability sets in after a certain number of cycles of the ac-drive depending on the strength of the parametric resonance, *i.e.* on the value of  $\sqrt{a} \simeq 1, 2, 3, \dots$ . Thereafter the system usually evolves through a sequence of different patterns (rhombi, stripes, etc.), composed of localized regions of high amplitude oscillations, before reaching a final configuration that may or may not result in a structure of definite symmetry.

Due to the sensitive response to very small changes in the parameters, determining stability regions for the different pattern geometries generally is a difficult task. However, in the case of a hard potential ( $\lambda = -1$ ), Fig.1 shows a limited area of  $(\varepsilon, \omega)$ -space in which distinct spatial patterns emerge and remain stable.

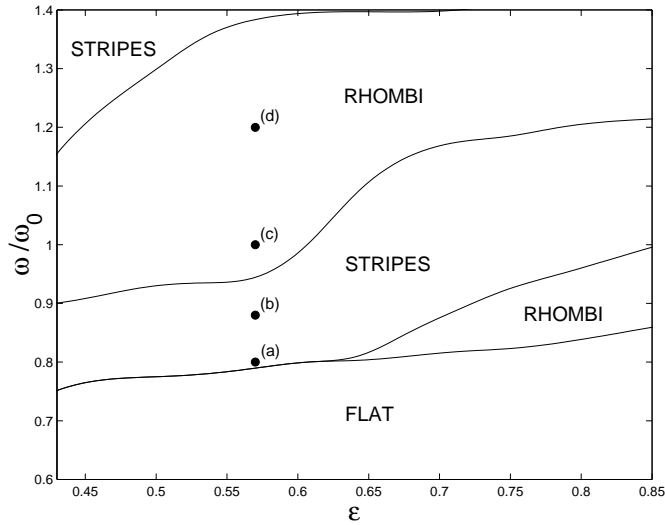


Figure 1 Stability diagram showing the stability boundaries between the possible patterns in the  $(\varepsilon, \omega)$ -plane. Parameters are  $\omega_0 = 0.75$ ,  $\lambda = -1$  (hard potential),  $\gamma = 0.05\omega_0$ . The four points refer to the specific spatial structures shown in Fig. 2.

This diagram is constructed following the full dynamics of the system for thousands of cycles. As in the case of Ref. [6], hysteresis is likely to occur but we do not pursue this further here. Figure 2 shows representative snapshots of the spontaneously emerging patterns corresponding to the points marked in Fig. 1.

The patterns consist of localized regions of high amplitude oscillations (i.e. intrinsic localized modes (ILM's)) residing on a background that oscillates at the frequency  $\omega$  of the ac-drive. In all the cases considered we have observed the natural result that patterns are only energetically sustained when the ILM,  $\omega_{ILM}$ , and driving,  $\omega$ , frequencies are commensurate, i.e.  $\omega_{ILM} = n\omega$ , where  $n$  is an integer. For the patterns displayed in Fig. 2,  $n = 2$ . Furthermore, the motion of the ILM's is exactly out of phase, meaning that at times where the background oscillation reaches its maximal excursion the ILM's attain their minimal amplitude such that at these points the state is completely homogeneous.

At a fixed driving  $\varepsilon$ , for increasing values of the frequency  $\omega$ , as in Fig. 1, we observe the following behavior: Due to the presence of the

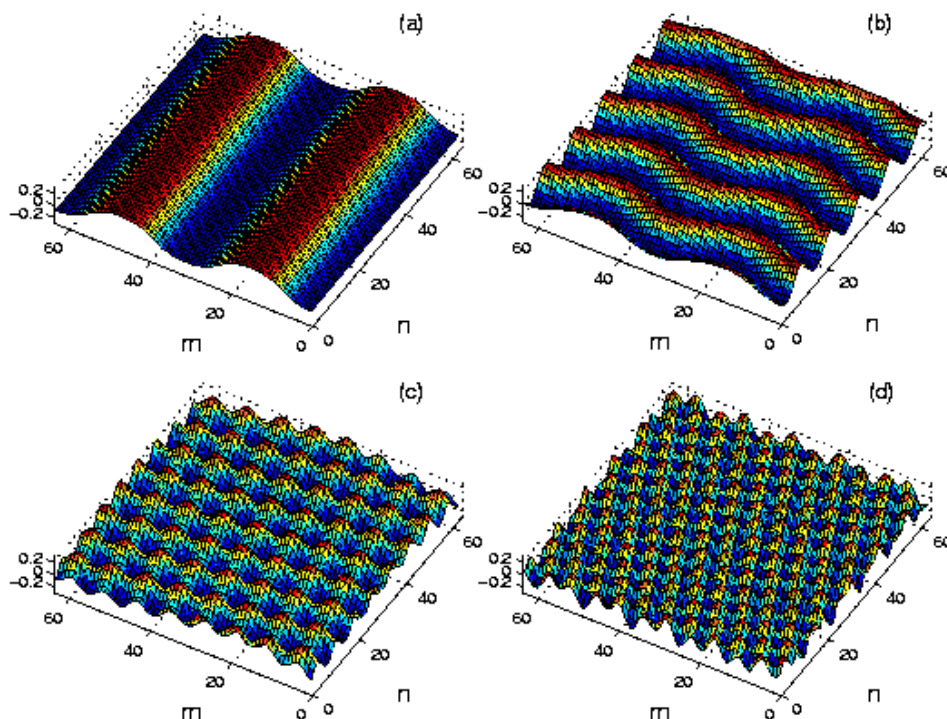


Figure 2 (Color) Snapshots of spatial patterns corresponding to the four points marked in Fig. 1 for  $\varepsilon = 0.57$ : (a) straight stripes ( $\omega = 0.8\omega_0$ ), (b) modulated stripes ( $\omega = 0.88\omega_0$ ), (c) rhombi ( $\omega = 1.0\omega_0$ ), (d) localized rhombi ( $\omega = 1.2\omega_0$ ).  $x_{n,m}$  is plotted along the vertical axes.

damping  $\gamma$ , at sufficiently small  $\omega$  the spatially homogeneous solution is stable towards all possible spatial modulations such that the *flat* state is sustained. However, for values near point (a) the system becomes unstable with respect to certain spatial modulations and spatial patterns in the form of broad stripes emerge (Fig. 2(a)). Increasing the frequency, these stripes become thinner and denser and begin to show an increasingly clear modulation (Fig. 2(b)). The characteristic length scale of these patterns is set by the size of the unstable  $\vec{k}$ -vector according to the above analysis. The nonlinear character of the system results in a transition towards a more isotropic geometry (rhombic) as the driving frequency is increased further (Fig. 2(c)). As in the case of the stripes, stronger localization of the ILM's arranged in the rhombic pattern (Fig. 2(d)) is observed for even larger driving frequencies. The angle between the sides of the rhombus' unit cell varies but for the hard potential it

is always close to  $\pi/2$ . For values of  $\varepsilon$  larger than those displayed in Fig. 1, the final mesoscopic patterns of the system dynamics are spatially disordered much like the phenomena observed in granular media [6]. It is important to realize that the length of the unstable wavevector determines the length-scales of the final patterns, while the symmetry of the patterns is determined by the nonlinearity of the system.

For the soft potential ( $\lambda = 1$ ) the variation of the amplitude  $\varepsilon$ , and the frequency  $\omega$ , of the ac-drive is particularly problematic since the dynamics in this case can lead to the development of catastrophic instabilities as one or several oscillators overcome the finite barrier in the quartic potential. In all the cases we have been able to simulate, the early stage time evolution of the system is characterized by the formation of ILM's regularly arranged in a square pattern. This spatial configuration, which is sustained for up to hundreds of cycles, seems always to suffer from a weak instability and eventually deforms into a rhombic pattern. In contrast to the case of the hard potential, with the soft potential the angle of the rhombus unit cell is always close to  $2\pi/3$  (so almost hexagonal). This difference can be understood by exploiting the analogy between the changes in the steady states of dissipative systems and phase transitions in systems at thermodynamic equilibrium[7].

### 3. DRY FRICTION

Spurred on by recent technological advances that have given new insight into frictional processes at the atomistic level [8], there have recently been many attempts to model atomic-scale friction using low-dimensional nonlinear models [9]. Many of these have been variations on driven one- or two-dimensional Frenkel-Kontorova (FK) type models, in which a chain or layer of interacting particles is subject to a periodic substrate potential and a driving force. Here (see also Ref. [10]) we describe one model which attempts to go one step further in coupling the nonlinear atomic dynamics which occur at the sliding interface with the essentially linear behavior deep in the bulk of the materials.

In the model the upper workpiece is represented by a one-dimensional chain of atoms at the interface coupled to an isotropic elastic medium. The lower workpiece is replaced by a sinusoidal substrate potential. Relative motion between the two workpieces is produced by translating the substrate potential at a fixed velocity,  $v$ . The two-dimensional (2D) medium is represented by a 2D array of 2D displacements  $u_1(i, j)$  and  $u_2(i, j)$ , for  $i$  and  $j$  spanning the medium. The geometry of the model is shown in Fig. 3.

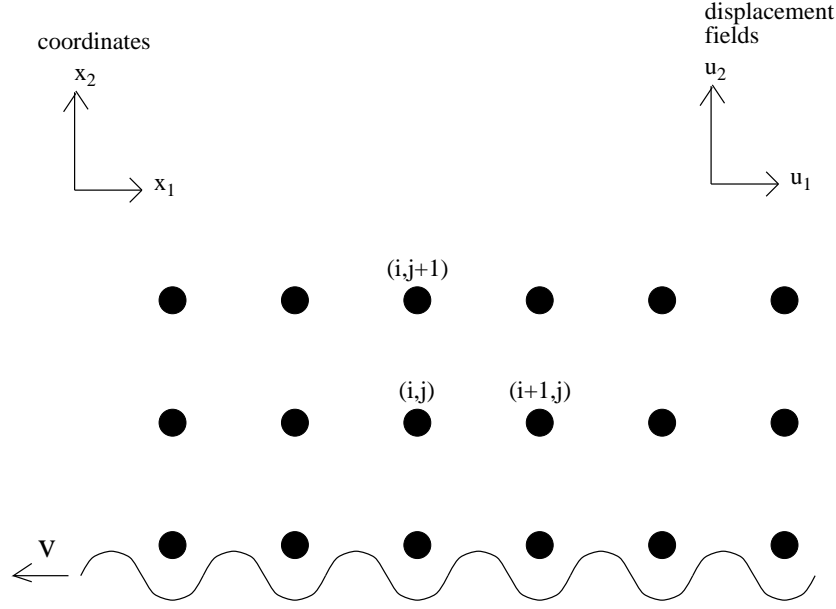


Figure 3 Geometry of the “isotropic elastic block” model of sliding friction described in the text.

The equations of motion of the model can be written as

$$\begin{aligned}
 \ddot{u}_1(i, j) &= (\lambda + \mu)(u_{1,11}(i, j) + u_{2,21}(i, j)) \\
 &\quad + \mu(u_{1,11}(i, j) + u_{1,22}(i, j)) + \frac{\delta_{1j}}{2\pi} \sin(2\pi(u_1(i, j) + vt)) \\
 \ddot{u}_2(i, j) &= (\lambda + \mu)(u_{2,22}(i, j) + u_{1,12}(i, j)) \\
 &\quad + \mu(u_{2,11}(i, j) + u_{2,22}(i, j)),
 \end{aligned} \tag{1.7}$$

where  $u_{l,mn}(i, j)$  is the discretized second derivative of the displacement component  $u_l$  at the site  $(i, j)$  in the directions  $m$  and  $n$ . The Lamé constants,  $\lambda$  and  $\mu$  were taken to be  $1/3$ , so that the longitudinal sound speed,  $c_l = 1$ . Notice that only the first layer of the block interacts directly with the substrate potential, confining the nonlinearity to the interface. These equations can be solved numerically to yield the long-time steady state behavior of the system at any given  $v$ .

For small enough velocities, i.e.  $v < v_c \approx 0.2$ , the block sticks to the substrate and will be dragged along with the same average velocity. For higher velocities,  $v > v_c$ , one observes that there is an initial jerk, the size of which depends on how close the block is to sticking to the substrate. After this jerk, the block oscillates around a fixed position. For perfectly uniform initial conditions (i.e. all  $u_1 = u_2 = 0$ ) and no noise

this persists as the steady state. However, when one allows for a small random perturbation on the uniform initial conditions, one observes that during the oscillation a certain wavelength modulation in the  $x_1$  direction is selected. This modulation grows until saturation. Then one observes that the block assumes a small non-zero velocity to reach the steady state. This time development can easily be followed by looking at a snapshot of the elastic energy. As can be seen in the Fig. 4(a), the leading wavefronts are practically flat, then the modulation develops until it saturates. One then observes that a periodic pattern develops in the elastic medium. Similar patterning has been observed in one-dimensional FK and sine-Gordon systems [11].

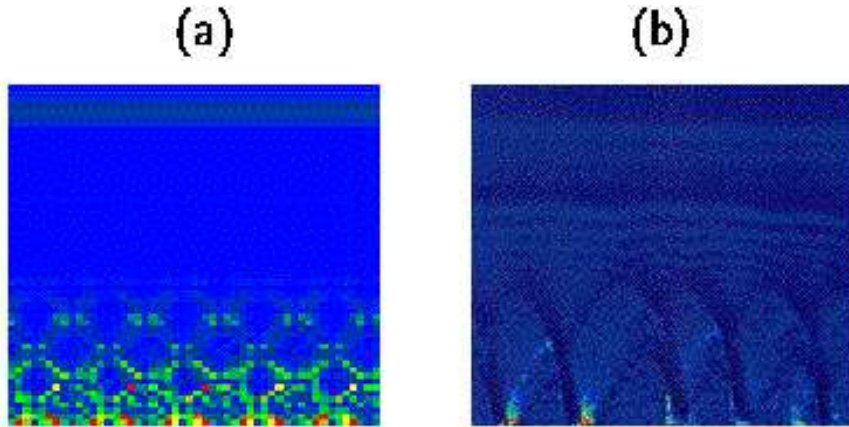


Figure 4 (Color) (a) Snapshot of the elastic energy of the model; (b) Snapshot of the potential energy of the 2D molecular dynamics simulations. (Both are color coded from blue at low values to red at high values.)

The selection of a particular wavelength parallel to the interface,  $k_{x_1}$ , is apparent in Fig. 4(a). This wavelength is chosen by the system matching the driving frequency of the moving substrate potential as closely as possible to the dispersion relation of the longitudinal waves of the elastic medium,  $\omega = c_l k_{x_1}$ . Perfect agreement is achieved in this process by the block adopting a small non-zero velocity,  $v_{block}$  so that the driving frequency is tuned to  $\pi v_{slip} = \pi(v - |\langle v_{block} \rangle|) = c_l k_{x_1}$ . (Angular brackets represent a time-averaged quantity.)

This effect of locking to the wavelength most closely matched to the driving frequency can be seen in the frictional behavior of the system. Fig. 5 shows the frictional force exerted by the substrate on the elastic block as a function of  $v$ . One sees regular portions of the curve, where one

particular wavelength is selected, separated by jumps where the system changes from one modulation wavelength to the next. So, the spatial patterning is reflected in the mechanical properties of the system.

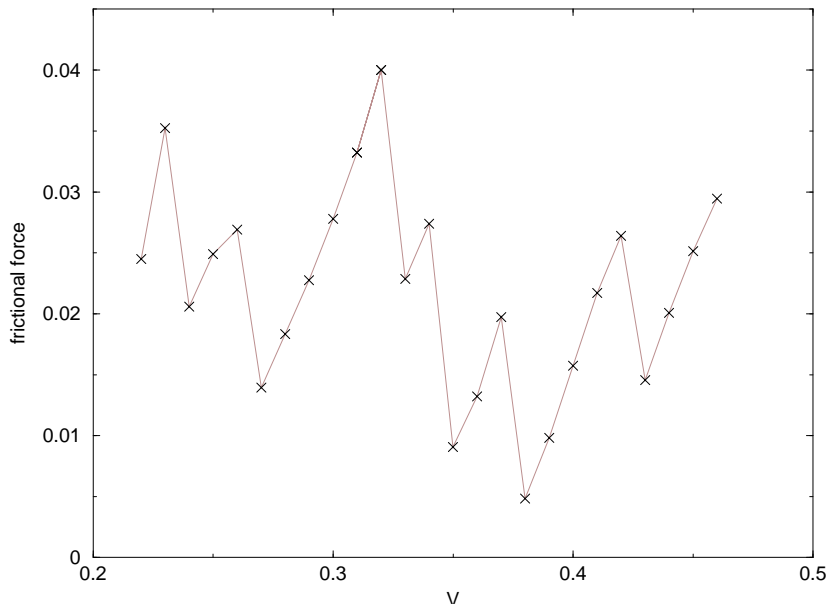


Figure 5 Plot of the frictional force as a function of substrate velocity,  $v$ .

Large-scale molecular dynamics (MD) simulations have been performed of the sliding of two 2D copper workpieces incorporating realistic embedded-atom potentials. An early-time snapshot of the potential energies of the atoms in the simulations is shown in Fig. 4(b), alongside a corresponding snapshot of the elastic energies for the model. It is evident that the simple model successfully reproduces the qualitative features of the early-time behavior of the MD simulations. In addition, the elastic block model is able to elucidate the *physical mechanism* behind the patterning observed in the large-scale MD simulations.

#### 4. PATTERNS ARISING FROM ELASTIC COMPATIBILITY

Martensitic structural transitions [1], especially those with unit cells related by continuous deformations (solid-solid phase transitions), exhibit a rich variety of temperature/stress induced microtextures [12, 13, 14]. For example, alloys such as FePd, and NiTi show the shape mem-

ory effect [15], transforming on cooling from a higher symmetry phase (‘austenite’), through nanometer-scale ‘tweed’ textures; to equal-width mesoscale ‘twins’ below the (‘martensite’) transition temperature  $T_0$ .

To understand martensitic transitions and textures in a Ginzburg-Landau (GL) approach based on the natural order parameter (OP), we need a treatment in terms of the physical strain variables alone. The OP is one or more components of a strain tensor  $\varepsilon_{\mu\nu}(\mu, \nu = x, y, z)$ ; not a true scalar. For simplicity, we consider here a 2D square-to-rectangle transformation [16, 17, 18, 19], with a rectangular or deviatoric strain as the OP. The non-OP strain components are implicit functions of the OP, through a compatibility (differential) equation [20]. Thus the apparently innocuous GL terms, harmonic in the non-OP components, are crucial: they generate two effective long-range anisotropic OP potentials: from the bulk and from the ‘habit-plane’ interfaces. The combined action of these *two* compatibility potentials plays a decisive role in the energetic competition between various OP textures, e.g. for temperatures  $T < T_0$ , oriented, *equal-width* twins are favored, emerging into the bulk from the habit plane. Our GL model includes alloy composition fluctuations as local internal micro-stresses, that induce tweed textures at  $T > T_0$ . We show that simple and local external stresses can generate complex and extended, multiscale structures throughout the system, that could play a role in shape memory. Thus we find that bulk/interface strain potentials induced by compatibility enable a unified description of spontaneously formed, and stress-induced martensitic textures, in a GL model in terms of the OP strain alone. Our GL model in 2D consists of (i) a triple-well potential  $F_0$ , as is usual for first order transitions, in the deviatoric strain OP [ $\epsilon = (1/\sqrt{2})(\varepsilon_{xx} - \varepsilon_{yy})$ ], (ii) harmonic (linear) elastic energy cost  $F_{cs}$  due to the compressional [ $e_1 = (1/\sqrt{2})(\varepsilon_{xx} + \varepsilon_{yy})$ ] and shear ( $e_2 = \varepsilon_{xy}$ ) strain that implicitly depend on the OP through compatibility; (iii) coupling of strain(s) to an external or internal (defect, dislocation) stress; (iv) second and fourth order strain gradient terms  $F_{grad}$  that give rise to multiscale competition; and (v) symmetry-allowed couplings  $F_{compos}$  of the (scalar) compositional fluctuations  $\tilde{\eta}(r)$  to the OP and its derivatives.

The (dimensionless) elastic energy in 2D is given with,  $\epsilon = \epsilon(r)$ , by:

$$F = F_0(\epsilon) + F_{grad}(\nabla\epsilon) + F_{cs}(e_1, e_2) + F_{compos}(\epsilon), \quad (1.8)$$

where the detailed expressions can be found in Ref. [21]. The dynamics of the continuous OP is assumed to be of the time dependent GL or relaxational type,

$$\dot{\epsilon}(r) = -\frac{\partial F(\{\epsilon(r), e_1(\epsilon(r)), e_2(\epsilon(r))\})}{\partial \epsilon(r)}, \quad (1.9)$$

where time  $t$  is scaled with a characteristic relaxation rate. The compression-shear (CS) strains  $e_1(r), e_2(r)$  are written in terms of the order parameter  $\epsilon(r)$  by solving the elastic compatibility (differential) equation. The analysis with six strain tensor components in 3D can be carried out [22], but for simplicity, we confine our discussion to 2D with a compatibility constraint, satisfied at all times [17, 23]:

$$\nabla^2 e_1(r) - \sqrt{8} \nabla_x \nabla_y e_2(r) = (\nabla_x^2 - \nabla_y^2) \epsilon(r). \quad (1.10)$$

For (Fourier-expandable) strains  $\epsilon(r)$  in the bulk, one obtains via the Lagrangian multiplier formalism [17] that  $e_1(\vec{k}), e_2(\vec{k})$  are proportional to  $\epsilon(\vec{k})$ , with  $\vec{k}$  dependent coefficients. An OP strain-strain potential  $F(\epsilon)_{cs} = F_{cs}^{(bulk)} + F_{cs}^{(surface)}$  replaces  $F_{cs}(e_1, e_2)$ , where  $F_{cs}^{(bulk)} = \sum_{\vec{k}} U^{(bulk)}(\vec{k}) |\epsilon(\vec{k})|^2$  and in  $\vec{k}$ -space

$$U^{(bulk)}(\vec{k}) = \frac{\frac{2A_1}{A_2} \left[ \frac{(k_x^2 - k_y^2)}{k^2} \right]^2}{1 + \frac{8A_1}{A_2} \frac{k_x^2 k_y^2}{k^4}}. \quad (1.11)$$

Here  $A_1$  and  $A_2$  are bulk and shear modulus, respectively. A similar expression can be derived for the surface contribution  $F_{cs}^{(surface)}$ .

In the numerical simulations reported below we take random initial conditions, a  $256 \times 256$  lattice, and periodic boundary conditions in both  $x$  and  $y$  directions to obtain relaxed textures  $\epsilon(r)$ . The red/blue/green color shades represent  $\epsilon$  positive/negative/zero OP strain values.

Figure 6 shows formation of low temperature  $T < T_0$  parallel-domain structures with only bulk compatibility included. Note that the structures have the proper  $45^\circ$  orientation (as in [17]) but are not true twins: there is no well defined width scale. In Fig. 6b we depict horizontal twin-like structures with only the surface compatibility term included. Now there is a dominant length scale (twin width) in the system but the ‘twins’ have rough interfaces and are not properly oriented. When *both* bulk and surface compatibility terms are included we obtain equally spaced, parallel, and properly oriented twins. The corresponding derived (deviatoric) OP strain field  $\tilde{\epsilon}(r)$  in the austenite [16] falls off as ‘decaying twins’ away from the habit plane, as depicted in Fig. 6(d).

Figure 7a shows how  $T \gg T_0$  austenite, evolves to twinned martensite, under a temperature quench to  $T < T_0$ . There is a growth process resulting in twinned martensite. Note the lenticular twin shapes, surrounding elastic field and the “skew-varicose” interface instability just before the twinning is complete. The latter instability is observed in many other contexts such as granular media and convective rolls in fluids [24]. The total compressional/shear strains, derivable from the bulk OP

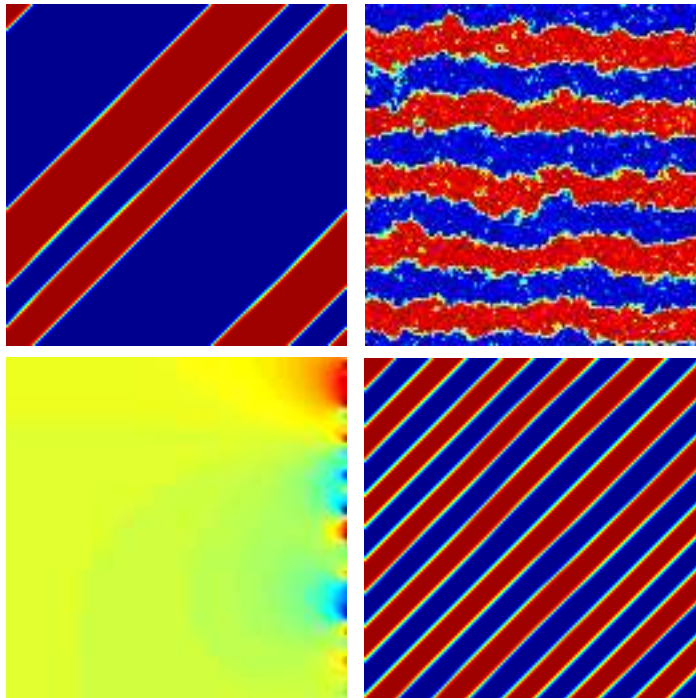


*Figure 6* (Color) Clockwise from upper left: (a) Oriented  $\pi/4$  parallel structure obtained from bulk compatibility only. (b) Unoriented ‘twins’ obtained from surface compatibility only. (c) Oriented twins with both bulk and surface compatibility present. (d) Corresponding elastic fringing field in the austenite.

strain through compatibility, as above, are not shown here. For  $T < T_0$ ,  $e_1, e_2$  are expelled from the bulk to the interface when equilibrium OP twins with  $\pi/4$  orientation finally emerge. By contrast, the  $T > T_0$  OP tweed shows  $e_1, e_2$  strains in the bulk, localized at the domain-wall crossing points. This is reminiscent of type-II superconductors, with  $T_0 \sim T_{c1}$ , and with twin (tweed) textures acting like Meissner (vortex) phases, expelling (allowing localized) shear strains that are analogous to transverse vector potentials.

Fig. 7b shows how (suitably seeded) twins can evolve under uniform external stress. The growth of (at least two generations of) hierarchical twinning is shown. A new generation of twins nucleates when the elastic strain between two preexisting twins exceeds a critical value. Branched twin-like structures may be seen where the fine twins meet the coarser ones.

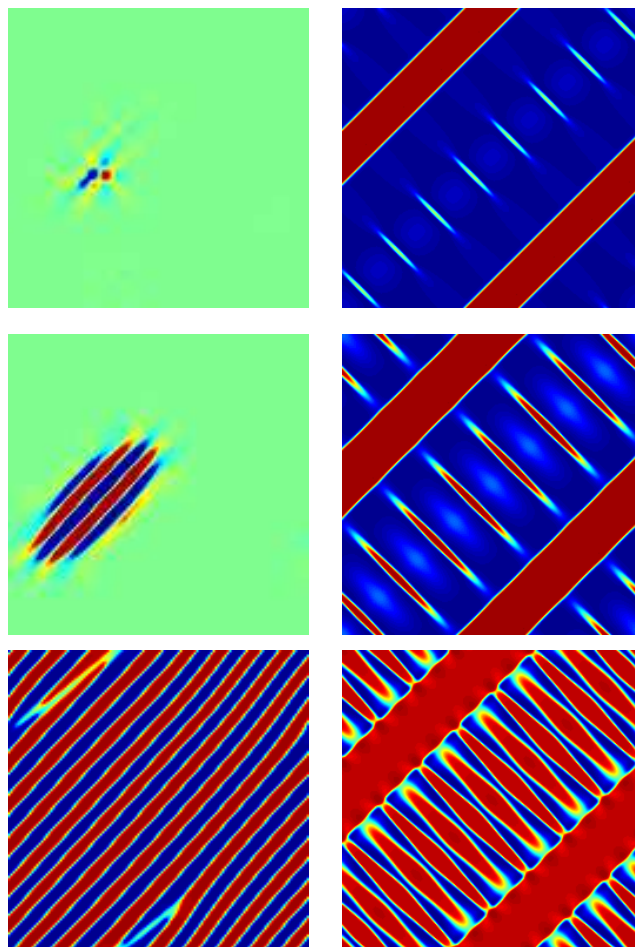


*Figure 7* (Color) Effect of a temperature quench and stress: (a) Left column, top down, a time sequence showing how a ‘temperature quench’ of austenite results in nucleation and growth of twinned martensite, (b) Right column, top down, a time sequence under external uniform stress (seeded) twins, inducing hierarchy and branching of twins.

## 5. CONCLUSIONS

By way of three quite different examples we have illustrated some of the salient features controlling mesoscopic patterns: Forced versus unforced environments; the effects of discrete lattice scales; the competitions between anisotropic short and long-range interactions; and the manifestation of constraints as source of long-range interactions. The re-

maintaining challenge, once one fully understands how to model systems at mesoscopic scales, is the length scale bridging: (i) To feed information in an appropriate and feasible way from experiments and microscopic models such as molecular dynamics simulations, electronic structure calculations etc. into the mesoscopic models. (ii) Use the information obtained from mesoscopic models as building components in understanding macroscopic behavior in the context of, for example, mechanical finite element models or the materials constitutive response.

## Acknowledgments

We gratefully acknowledge fruitful discussions with V. Bortolani, J. Hammerberg, B.L. Holian, B.A. Malomed, R. Mikulla, and S.R. Shenoy. Work at Los Alamos National Laboratory is performed under the auspices of the US DOE.

## References

- [1] Z. Nishiyama, *Martensitic Transformations* (Academic, New York, 1978).
- [2] A. Vanossi, K. Ø. Rasmussen, A. R. Bishop, B. A. Malomed, and V. Bortolani, *Phys. Rev. E*, **62**, 7353 (2000).
- [3] The two-dimensional version of Eq.(1.1) is  $\ddot{x}_{n,m} + \gamma\dot{x}_{n,m} + \omega_0^2 x_{n,m} = x_{n+1,m} - 4x_{n,m} + x_{n-1,m} + x_{n,m-1} + x_{n,m+1} + \lambda x_{n,m}^3 + \epsilon \cos \omega t$ , where the parameters have the interpretation given in connection with Eq. (1.1).
- [4] V. I. Arnold, *Mathematical Methods of Classical Mechanics*, (Springer, New York, 1997).
- [5] M. Abramowitz and I. A. Stegun, *Handbook of mathematical functions with formulas, graphs, and mathematical tables*, (U.S. Govt. Print. Off., Washington, D.C., 1964).
- [6] F. Melo, P. Umbanhowar, and H. L. Swinney, *Phys. Rev. Lett.* **72**, 172 (1994); **75**, 3838 (1995); P. Umbanhowar, F. Melo and H. L. Swinney, *Nature*, **382**, 793 (1996); C. Bizon, M. D. Shattuck, J. B. Swift, W. D. McCormick, H. L. Swinney, *Phys. Rev. Lett.* **80**, 57 (1998).
- [7] B. A. Malomed, A. A. Nepomnyashcii, and T. I. Tribekskii, *Zh. Eksp. Teor. Fiz.* **96**, 684 (1989). [*Sov. Phys. JETP* **69**, 388 (1989)].
- [8] B. Brushan, J. N. Israelachvili, and U. Landman, *Nature (London)* **374**, 607 (1995).
- [9] B. N. J. Persson, *The Physics of Sliding Friction*, (Springer, Heidelberg, 1998); M. O. Robbins and M. H. Müser, in *Handbook of Modern Tribology* (CRC Press, 2000).

- [10] J. Röder, A. R. Bishop, B. L. Holian, J. E. Hammerberg, and R. P. Mikulla, *Physica D* **142**, 306 (2000).
- [11] J. Röder, J. E. Hammerberg, B. L. Holian, and A. R. Bishop, *Phys. Rev. B* **57**, 2759 (1998); J. C. Ariyasu and A. R. Bishop, *Phys. Rev. B* **35**, 3207 (1987).
- [12] L. E. Tanner, A. R. Pelton, and R. Gronsby, *J. Phys. (Paris)* **43**, C4-169 (1982).
- [13] R. Oshima, M. Sugiyama, and F.E. Fujita, *Metall. Trans. A* **19**, 803 (1988).
- [14] M. Sugiyama, Ph. D. Thesis, Osaka University, 1985.
- [15] *Shape Memory Effect in Alloys*, J. Perkins, ed. (Plenum, New York, 1975); *Shape Memory Materials*, eds. K. Otsuka, and C. M. Wayman, (Cambridge University Press, Cambridge, 1998).
- [16] G. R. Barsch, B. Horovitz, and J. A. Krumhansl, *Phys. Rev. Lett.* **59**, 1251 (1987); B. Horovitz, G. R. Barsch, and J. A. Krumhansl, *Phys. Rev. B* **43**, 1021 (1991).
- [17] S. Kartha, T. Kastàn, J.A. Krumhansl, and J.P. Sethna, *Phys. Rev. Lett.* **67**, 3630 (1991); J. P. Sethna et al., S. Kartha, T. Kastàn, and J.A. Krumhansl, *Phys. Scripta* **T42**, 214 (1992); S. Kartha, J.A. Krumhansl, J.P. Sethna, and L. K. Wickham, *Phys. Rev. B* **52**, 803 (1995).
- [18] A. E. Jacobs, *Phys. Rev. B* **31**, 5985 (1985); **46**, 8080 (1992); **52**, 6327 (1995).
- [19] A. Saxena, S. R. Shenoy, A. R. Bishop, Y. Wu, and T. Lookman, *Physica A* **239**, 18 (1997).
- [20] D. S. Chandrasekharaiyah and L. Debnath, *Continuum Mechanics* (Academic Press, San Diego, 1994), p 218.
- [21] S. R. Shenoy, T. Lookman, A. Saxena, and A. R. Bishop, *Phys. Rev. B*, **60**, R12537 (1999).
- [22] K. Ø. Rasmussen, T. Lookman, A. Saxena, A. R. Bishop, and R. C. Albers, <http://xxx.lanl.gov/abs/cond-mat/0001410>.
- [23] W. C. Kerr, M. G. Killough, A. Saxena, P. J. Swart, A. R. Bishop, *Phase Trans.* **69**, 247 (1999).
- [24] J. R. deBruyn, C. Bizon, M. D. Shattuck, D. Goldman, J. B. Swift, H. L. Swinney, *Phys. Rev. Lett.* **81**, 1421 (1998).